

Article

Open Access



Dealloying-derived Fe-doped Ni(OH)₂/Ni foils as self-supported oxygen evolution reaction catalysts

Zheng Wang¹, Zhenhan Li¹, Yang Chao¹, Yu Cui¹, Xin He¹, Ping Liang^{1,*}, Chi Zhang^{1,*}, Zhonghua Zhang²

¹School of Applied Physics and Materials, Wuyi University, Jiangmen 529020, Guangdong, China.

²Key Laboratory for Liquid-Solid Structural Evolution and Processing of Materials (Ministry of Education), School of Materials Science and Engineering, Shandong University, Jinan 250061, Shandong, China.

*Correspondence to: A/Prof. Chi Zhang, School of Applied Physics and Materials, Wuyi University, Yingbin Road 99, Jiangmen 529020, Guangdong, China. E-mail: ch.zhang@outlook.com; A/Prof. Ping Liang, School of Applied Physics and Materials, Wuyi University, Yingbin Road 99, Jiangmen 529020, Guangdong, China. E-mail: ping_liang@126.com

How to cite this article: Wang Z, Li Z, Chao Y, Cui Y, He X, Liang P, Zhang C, Zhang Z. Dealloying-derived Fe-doped Ni(OH)₂/Ni foils as self-supported oxygen evolution reaction catalysts. *Energy Mater* 2022;2:200019. <https://dx.doi.org/10.20517/energymater.2022.19>

Received: 24 Apr 2022 **First Decision:** 7 May 2022 **Revised:** 26 May 2022 **Accepted:** 30 May 2022 **Published:** 13 Jun 2022

Academic Editors: Yuping Wu, Wei Tang **Copy Editor:** Jia-Xin Zhang **Production Editor:** Jia-Xin Zhang

Abstract

Dealloying has been an essential technique for developing nanostructured catalysts for the oxygen evolution reaction (OER). Self-supported active catalysts can be fabricated through an alloying-dealloying process on metal foil surfaces. This study uses a Ga-assisted alloying-dealloying strategy combined with electrooxidation and heteroatom doping to fabricate a Fe-doped Ni(OH)₂/Ni self-supported OER catalyst. We find that the surface phase compositions and dealloyed structures can be adjusted by controlling the reaction-diffusion temperature and time. The optimized O-Ni-Fe/200-3 catalyst shows an overpotential of 318 mV to activate a 10 mA cm⁻² current density with a Tafel slope of 60.60 mV dec⁻¹. *Ex-situ* characterization of the catalyst proves that Fe doping promotes the formation of active NiOOH, which contributes to the excellent OER activity. This study extends the Ga-assisted alloying-dealloying strategy and demonstrates the possibility of controlling the microstructure of dealloyed materials by changing the reaction-diffusion conditions.

Keywords: Dealloying, reaction diffusion, oxygen evolution reaction, Ni(OH)₂

INTRODUCTION

Hydrogen (H₂) is an eco-friendly energy source with a high gravimetric energy density that is vital for a low-



© The Author(s) 2022. **Open Access** This article is licensed under a Creative Commons Attribution 4.0 International License (<https://creativecommons.org/licenses/by/4.0/>), which permits unrestricted use, sharing, adaptation, distribution and reproduction in any medium or format, for any purpose, even commercially, as long as you give appropriate credit to the original author(s) and the source, provide a link to the Creative Commons license, and indicate if changes were made.



carbon future. Electrochemical water splitting is a promising and efficient technique to transform electricity into H₂. In the electrochemical water-splitting process, high-efficiency catalysts are necessary to promote the energy conversion rate of H₂ production^[1,2]. In particular, in the anodic process, the oxygen evolution reaction (OER) suffers from sluggish kinetics, which results in massive electricity consumption to produce H₂^[3]. Noble metal catalysts, such as Pt, Ru, Ir, and their compounds, have been commercially utilized to increase the electrocatalytic efficiency^[4-7].

The search for catalysts from earth-abundant elements, especially those from the first row of 3d transition metals, has attracted significant attention from researchers. Ni, Co, Fe, and Mn-based materials, e.g., alloys^[8,9], oxides^[10-12], (oxy)hydroxides^[3,13,14], and chalcogenides^[15,16], are among the most promising candidates for catalyzing the OER. Among them, NiFe-based (oxy)hydroxides have the potential to be industrialized due to the abundant reserves of Ni and Fe elements^[3,9]. Substantial efforts have been made to study the catalytic mechanisms and enhance the performance of such NiFe-based (oxy)hydroxides, especially to investigate the role of Fe doping in Ni-based materials. For instance, Trotochaud *et al.* found that via coprecipitation with Fe, the conductivity of Ni (oxy)hydroxides increased distinctly and the Fe impurities were responsible for the improved activity of aged Ni (oxy)hydroxides^[14]. Friebel *et al.* stressed the importance of the Fe³⁺ cation in the OER performance of γ -Ni_{1-x}Fe_xOOH as they act as the active sites in γ -Ni_{1-x}Fe_xOOH instead of Ni³⁺^[17]. Zhang *et al.* observed the transformation of Fe₂O₃-Ni(OH)₂ to NiFe₂O₄-NiOOH during the OER via *in-situ* Raman spectroscopy^[18]. The influence of the Fe content on the performance of Ni-based materials must also be addressed. Studies have reported that trace Fe impurities from a KOH solution could significantly improve the OER activity^[14,19]. Klaus *et al.* found that aging a Ni(OH)₂ film in the unpurified electrolyte after five weeks can lead to more than 20% Fe incorporation^[20].

Generally, powdery catalysts are only synthesized for lab-scale studies. Binders and carbon powders are necessary when preparing the catalyst ink for the OER test, which affects the proper assessment of the catalytic performance^[4]. In contrast, a self-supported electrode can avoid such issues. Ni foams or foils have been extensively used as supporting substrates for oxygen/hydrogen evolution reaction catalysts^[21]. Through a hydro/solvothermal, chemical vapor deposition, or electrodeposition method, metal (oxy)hydroxides can be grown on a Ni substrate as self-supported catalysts^[22-25]. In addition, anodization is also a powerful technique to modify the surface properties of Ni foam or foil. By applying an anodization potential of 50 V in oxalate acid, C-doped NiO was formed on the Ni foam surface with excellent activity^[26]. Surface alloying/dealloying offers another opportunity to generate active sites on free-standing Ni. Dealloying is generally used as a top-down strategy to fabricate nanoporous metals. Though the dealloyed metals are mostly powdery, self-standing dealloyed materials can be achieved using metallic glasses as precursors^[27,28]. Recently, our group proposed a liquid metal Ga-assisted alloying/dealloying method to transform the surface of metal foils, e.g., Ni, Co, Cu, Au, and Ag, into a nanostructured layer^[29,30]. In this method, the alloying process is controlled by the reaction diffusion between metals, and the compositions and structures of the dealloyed metals can be adjusted by optimizing the dealloying process and post-treatment.

Herein, a Ga-assisted alloying/dealloying method combined with post-electrooxidation is applied to form a Fe-doped Ni(OH)₂/Ni foil. The alloying process of Ga and Ni is studied by controlling the heat treatment temperature and time. Different Ga-Ni phase compositions and alloying depths are obtained by changing the temperature and time. A Ni columnar array structure is formed after dealloying the Ga-Ni alloy layer in a 0.2 or 2 M NaOH solution. Further electrooxidation of the dealloyed foils in a Fe³⁺-containing alkaline electrolyte results in the formation of an Fe-doped Ni(OH)₂ layer on the surface. The as-fabricated catalysts are self-supporting and have good performance in OER catalysis. The optimized Fe-doped Ni(OH)₂/Ni foils deliver an overpotential of 318 mV at 10 mA cm⁻² and long durability of at least 10 h.

EXPERIMENTAL

Preparation of nanostructured nickel foil

Ni foils (99.9 wt.%) were cleaned by soaking in a 1 wt.% HCl solution for 30 min, followed by washing with deionized water and alcohol at least 3 times. A certain amount of Ga ingot (99.99 wt.%) was placed on a hotplate at 50 °C to maintain the liquid state. A paintbrush was used to brush liquid Ga onto the dried Ni foil, which was then annealed in a vacuum to form Ga-Ni alloys via reaction diffusion. The amount of painted Ga was measured as $\sim 8.9 \text{ mg cm}^{-2}$. The annealing was controlled at 150, 200, and 250 °C for 3 h to study the effect of temperature on the reaction-diffusion process. The effect of annealing time was also investigated by maintaining the annealing at 200 °C for 1, 3, and 6 h. The samples were labeled as Ga-Ni/X-Y, where X and Y refer to the temperature and time, respectively, e.g., Ga-Ni/200-3 was obtained by annealing the foil at 200 °C for 3 h. The prepared alloy foil was dealloyed in a 2 M NaOH solution at 80 °C until no bubbles appeared. The dealloyed Ni foil, labeled as D-Ni/X-Y following the above naming rule, was washed and dried in a vacuum at room temperature. The D-Ni/200-3 foil was then electrooxidized in a 0.1 M KOH solution using repeated cyclic voltammetry (CV) between 1 and 2 V *vs.* a reversible hydrogen electrode (RHE) for 50 cycles at 50 mV s^{-1} to obtain O-Ni/200-3. The Fe-doped sample (O-Ni-Fe/200-3) was achieved via electrooxidation of the D-Ni/200-3 foil in a 0.1 M KOH solution containing 0.1 M $\text{Fe}(\text{NO}_3)_3 \cdot 9\text{H}_2\text{O}$. The above electrooxidation process was conducted using a three-electrode system. A Pt electrode, a Ag/AgCl electrode, and the D-Ni/200-3 foil were used as the counter, reference, and working electrodes, respectively.

Characterization of catalysts

The phase compositions of the samples were investigated by X-ray diffraction (XRD, PANalytical X'pert Pro). A field-emission scanning electron microscope (SEM, Zeiss Sigma 500) and transmission electron microscope (TEM, FEI Tecnai G2 F20) were used to obtain the microstructures of the samples. Selected area electron diffraction (SAED), high-resolution transmission electron microscopy (HRTEM), and scanning transmission electron microscopy-energy dispersive spectroscopy (EDS) mapping were also used to study the nature of the crystallinity and composition of the samples. X-ray photoelectron spectroscopy (XPS, Thermo Scientific) was used to characterize the surface element states of the samples using monochromatic Al $K\alpha$ radiation.

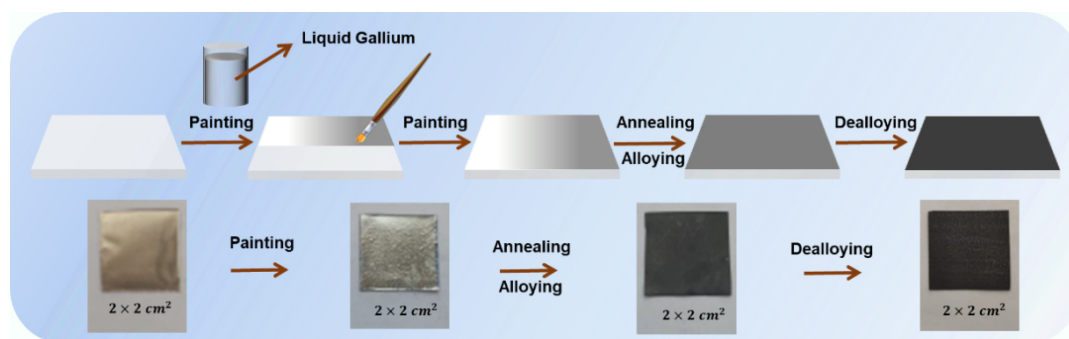
Electrochemical measurements

A three-electrode cell was used for the electrochemical measurements on a Bio-Logic SP-240 electrochemical workstation. The as-synthesized Ni foils were used as the working electrode ($0.5 \times 0.5 \text{ cm}^2$). The counter and reference electrodes were graphite rod and Ag/AgCl (saturated KCl filled), respectively. All potentials measured were converted to the RHE scale, according to $E \text{ (vs. RHE)} = E \text{ (vs. Ag/AgCl)} + 0.0591 \text{ pH} + 0.197$.

The linear sweep voltammetry (LSV) curves were carried out in an O_2 -saturated 1.0 M KOH electrolyte with a sweep rate of 5 mV s^{-1} . All LSV curves were *iR*-compensated to exclude the influence of the solution resistance. CV curves were recorded at 0.0-0.6 V *vs.* Ag/AgCl with various sweep rates to analyze the number of active sites. Electrochemical impedance spectroscopy (EIS) was conducted on the same electrolyte from 10^6 to 0.1 Hz at 0.6 V *vs.* Ag/AgCl at 1600 rpm with an excitation voltage of 5 mV.

Results and discussion

The Ni foils with a nanostructured layer on the surface were obtained from a facile Ga painting-alloying-dealloying strategy^[30], as illustrated in [Scheme 1](#). After painting Ga on the surface of the Ni foil, the subsequent annealing treatment promoted the reaction diffusion between Ga and Ni. The XRD patterns in [Supplementary Figure 1](#) display the phase composition before annealing, where the Ga (PDF #05-0601) and



Scheme 1. Schematic illustration and photographs showing the fabrication process for the dealloyed foil.

Ni phases (PDF #04-0850) can be observed. The reaction diffusion may generate various Ga-Ni phases by adjusting the annealing temperature and time. Based on this assumption, we annealed the Ga-painted Ni foil at 150, 200, and 250 °C for 3 h and at 200 °C for 1, 3, and 6 h to demonstrate the change in phase compositions. The XRD patterns in [Figure 1A](#) exhibit that, after being annealed at 150 °C for 3 h, Ga_4Ni (PDF #37-1095) and Ni (PDF #04-0850) phases are found on the foil, indicating that all the Ga was transformed into the Ga_4Ni alloy.

Increasing the annealing temperature leads to impurity phases, such as Ga_3Ni_2 (PDF #65-7366) at 200 °C and Ga_4Ni_3 (PDF # 65-9741) at 250 °C for 3 h. The atomic ratio of Ga to Ni is 1.50 for Ga_3Ni_2 and 1.33 for Ga_4Ni_3 , indicating that less Ga reacted with Ni in the deeper areas of the Ni foil. To probe the effect of annealing time, we annealed the sample for 1, 3, and 6 h at 200 °C [[Figure 1B](#)]. After 1 h of annealing at 200 °C, the Ga phase was still detected on the foil surface, while all Ga was transformed to Ga_4Ni after 3 and 6 h. [Supplementary Figure 2A-H](#), [Supplementary Figure 3A-H](#), and [Supplementary Figure 4A-H](#) display the SEM images and EDS mapping and spectra for Ga-Ni/200-1, Ga-Ni/200-3, and Ga-Ni/200-6, respectively. With the annealing time extended from 1 to 6 h, the content of Ga on the foil surface decreased, indicating the gradual diffusion of Ga into the Ni foil.

As previously reported, the Ga-X (X = Co or Ni) alloys could be dealloyed in NaOH solutions^[30,31]. Herein, we applied 2 M NaOH as the dealloying electrolyte. The phase compositions of the as-dealloyed samples are exhibited in [Figure 1C](#) and [D](#). Both the D-Ni/150-3 and D-Ni/200-3 samples were fully dealloyed with only the Ni phase retained. While for D-Ni/250-3, the Ga_3Ni_2 phase could still be detected after dealloying. However, the Ga-Ni alloy layer can be dealloyed entirely for the samples annealed at 200 °C for 1, 3, and even 6 h. The annealing temperature influences the phase compositions, which may further affect the microstructure after dealloying. As shown in [Figure 2A-C](#), a cubic structure with an edge length of $\sim 2 \mu\text{m}$ was obtained for the D-Ni/150-3 sample. D-Ni/200-3 and D-Ni/250-3 show columnar arrays after being dealloyed in 2 M NaOH. The thickness of the dealloyed layer is measured as $\sim 5.5 \mu\text{m}$ for D-Ni/200-3 [[Figure 2D](#)] and the EDS results prove that there is still $\sim 10.0 \text{ at.}\%$ Ga retained after dealloying [[Figure 2E](#) and [F](#)].

The electrolytes, dealloying time, and temperature affect the dealloying behavior and structural features of the dealloyed metals^[32]. To evaluate the influence of the concentration of the dealloying electrolyte, we also used a 0.2 M NaOH solution as the dealloying electrolyte. Only D-Ni/150-3 can be fully dealloyed in such a dilute alkaline solution, while the Ga_4Ni phase was retained after dealloying the D-Ni/200-3 sample, and both Ga_4Ni and Ga_3Ni_2 were detected for the D-Ni/250-3 sample [[Supplementary Figure 5](#)]. Similar structures were found from the samples after dealloying in 0.2 M NaOH [[Supplementary Figure 6A-C](#)].

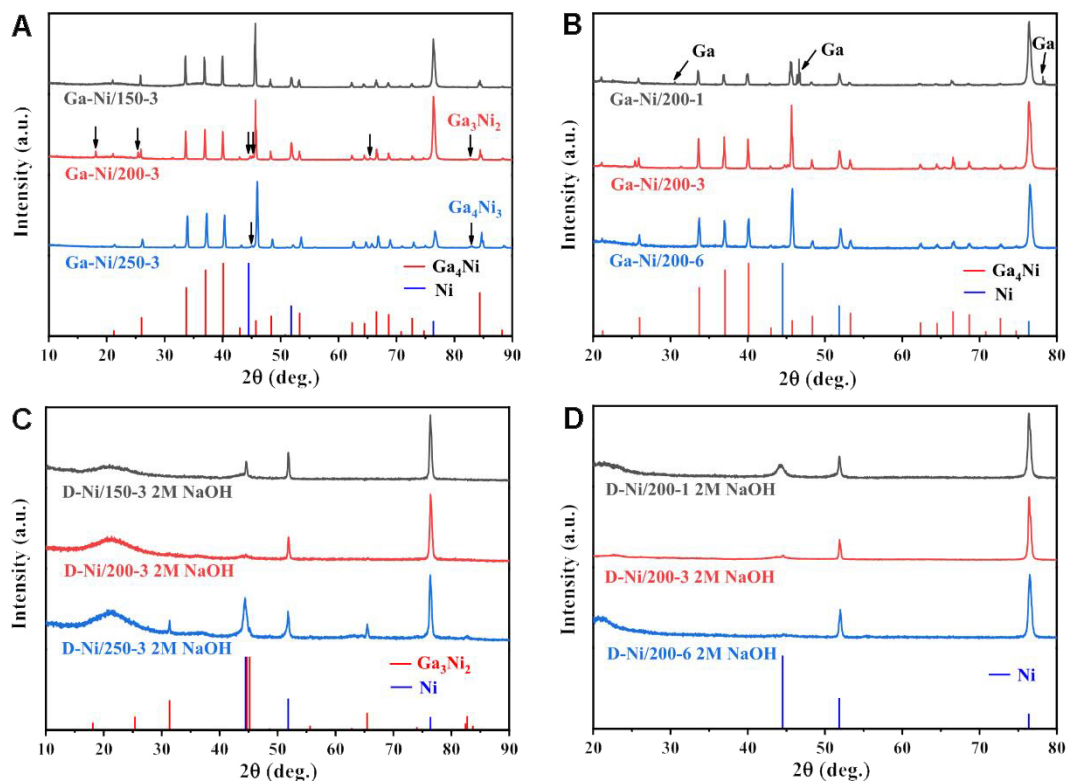


Figure 1. XRD patterns of (A) Ga-Ni alloy foil annealed at 150, 200, and 250 °C for 3 h, (B) Ga-Ni alloy foil annealed at 200 °C for 1, 3, and 6 h and dealloyed Ga-Ni alloy foil in 2 M NaOH, (C) D-Ni/150-3, D-Ni/200-3 and D-Ni/250-3 and (D) D-Ni/200-1, D-Ni/200-3 and D-Ni/200-6. XRD: X-ray diffraction.

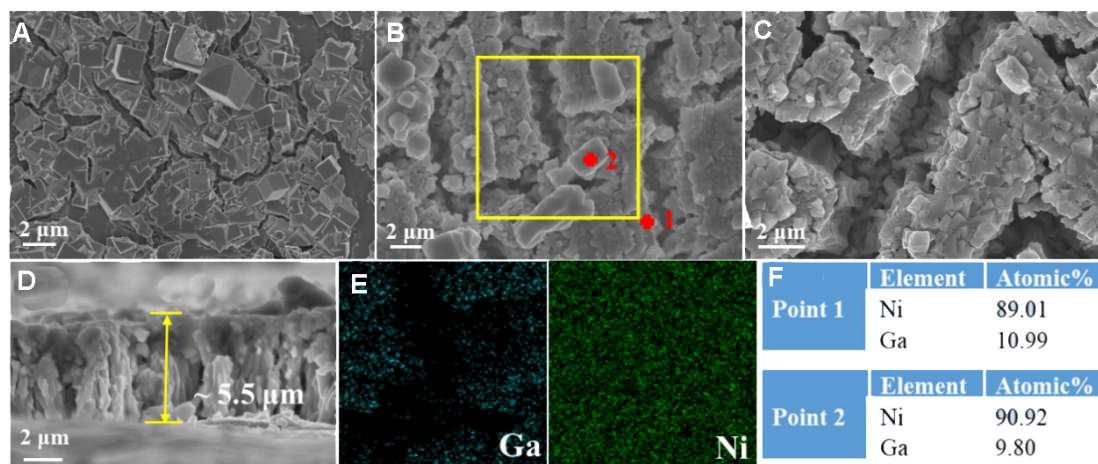


Figure 2. Surface microstructures of (A) D-Ni/150-3, (B) D-Ni/200-3, and (C) D-Ni/250-3 dealloyed in 2 M NaOH. (D) Cross-section view of D-Ni/200-3. (E) EDS elemental distribution corresponding to the yellow square area in (B). (F) Elemental ratios obtained from EDS point scan corresponding to points 1 and 2 in (B). EDS: Energy dispersive spectroscopy.

Furthermore, the EDS elemental distribution mapping displays almost only Ni in the D-Ni/150-3 sample [Supplementary Figure 6G]. Ga and Ni co-exist in the dealloyed zone for the D-Ni/200-3 and D-Ni/250-3 samples [Supplementary Figure 6H and I]. Taking D-Ni/200-3 as an example, the content of Ga increases

gradually from 17.89 at.% near the surface to 64.36 at.% at the interface [Supplementary Figure 6E]. Moreover, only a ~ 6 μm deep area was dealloyed in 0.2 M NaOH for D-Ni/250-3, as shown in Supplementary Figure 6F and I. From Supplementary Figure 6D-F, we can also observe the relation between the diffusion length and the annealing temperature. The Ga-Ni mutual diffusion length (d) increases with the annealing temperature (T), namely, from ~ 3.0 to ~ 5.8 μm and finally to ~ 14 μm for 150, 200, and 250 $^{\circ}\text{C}$, respectively. The results may guide the controllable fabrication of alloying layers by changing the annealing temperature. The above XRD and SEM analysis revealed that both the annealing temperature and time influenced the phase composition of the Ga-Ni alloying layer, which further affected the dealloying behavior in the NaOH solutions. The alloying layer can be entirely dealloyed in a 2 M NaOH solution, while some Ga-Ni phases were reserved using a 0.2 M NaOH solution. In the following discussion, we focus on the further treatment and application of the dealloyed foils using D-Ni/200-3 as an example.

An electrooxidation method via CV cycling was applied to generate an OER active $\text{Ni}(\text{OH})_2$ layer on the D-Ni/200-3 foil^[31,33]. The electrochemical feature of the first cycle is different from the rest of the cycles, indicating the irreversible oxidation process, which may create a $\text{Ni}(\text{OH})_2$ layer on the Ni surface (O-Ni/200-3) [Supplementary Figure 7A and B]. Fe doping has proved to be efficient in enhancing the OER performance of $\text{Ni}(\text{OH})_2$ -based catalysts^[14,34], so the Fe-doped O-Ni-Fe/200-3 foil was obtained by adding 0.1 M $\text{Fe}(\text{NO}_3)_3 \cdot 9\text{H}_2\text{O}$ in the 0.1 M KOH electrolyte during electrooxidation. The XRD patterns in Figure 3A of O-Ni/200-3 and O-Ni-Fe/200-3 present diffraction peaks of Ni (PDF # 04-0850) without obvious signals of $\text{Ni}(\text{OH})_2$. After Fe doping, a slight negative peak shift is observed, ascribed to the lattice expansion with Fe incorporation^[35]. We also used Raman spectroscopy to investigate the crystal structure change after Fe doping, with no noticeable difference observed [Supplementary Figure 8].

The surface chemical states of the catalysts were analyzed through XPS. The full-scan survey reveals the presence of Ni and O in D-Ni/200-3 and O-Ni/200-3, with Fe also observed in the O-Ni-Fe/200-3 sample [Figure 3B]. From the XPS survey [Supplementary Table 1], the surface atomic concentration ratio of Fe to Ni is estimated to be 0.32. If we assume that all Ni exists in $\text{Ni}(\text{OH})_2$, Fe occupies 15.95 wt.% of the total weight [Fe dopants and $\text{Ni}(\text{OH})_2$]. Considering that partial Ni forms NiOOH on the surface, the concentration of Fe would be less than 15.95 wt.%, lying in the optimal composition for NiFe-based catalysts^[17,20,36]. The deconvoluted O 1s peaks at 531.4 eV correspond to OH, indicating the formation of $\text{Ni}(\text{OH})_2$ on the surface of nanostructured Ni after dealloying. An extra peak at ~ 529.8 eV is present for the dealloyed sample, which might be due to the formation of the Ni-O phase after dealloying the Ni-based alloys in NaOH solutions^[37].

After CV cycling, all Ni-O phase was transformed into $\text{Ni}(\text{OH})_2$, as confirmed by the O 1s spectra of O-Ni/200-3 in Figure 3C. When Fe ions are present during the CV cycling, the O 1s spectrum again shows the peak at ~ 529.7 eV. It has been reported that trace Fe ions favor the formation of β - NiOOH , which might account for the existence of Ni-O in the O 1s spectrum of O-Ni-Fe/200-3^[38]. The Ni 2p spectrum of D-Ni/200-3 shows binding energies at 873.2 and 855.6 eV, representing Ni 2p_{1/2} and Ni 2p_{3/2} from $\text{Ni}(\text{OH})_2$, respectively [Figure 3D]^[39]. The binding energy at 852.5 eV refers to metallic Ni (Ni^0)^[40]. After CV cycling in 1 M KOH, Ni^0 is absent, suggesting the full oxidation of surface Ni. Moreover, Ni 2p_{3/2} from O-Ni/200-3 can be deconvoluted into Ni^{3+} at 855.4 eV and Ni^{2+} at 857.3 eV. The concentration of Ni^{2+} and Ni^{3+} can be calculated as 76.8 at.% and 23.2 at.%, respectively. After Fe doping, the binding energy of Ni 2p_{3/2} shifts positively from ~ 855.4 to ~ 855.7 eV, indicating the Fe incorporation in $\text{Ni}(\text{OH})_2$ ^[41]. The concentration of Ni^{3+} also increases to 26.7 at.% in the O-Ni-Fe/200-3 sample, further demonstrating the promotion effect of Fe on the generation of NiOOH ^[38]. The Fe 2p_{3/2} envelope can be fitted into Fe^{2+} at 711.1 eV and Fe^{3+} at 713.7 eV [Figure 3E]^[42].

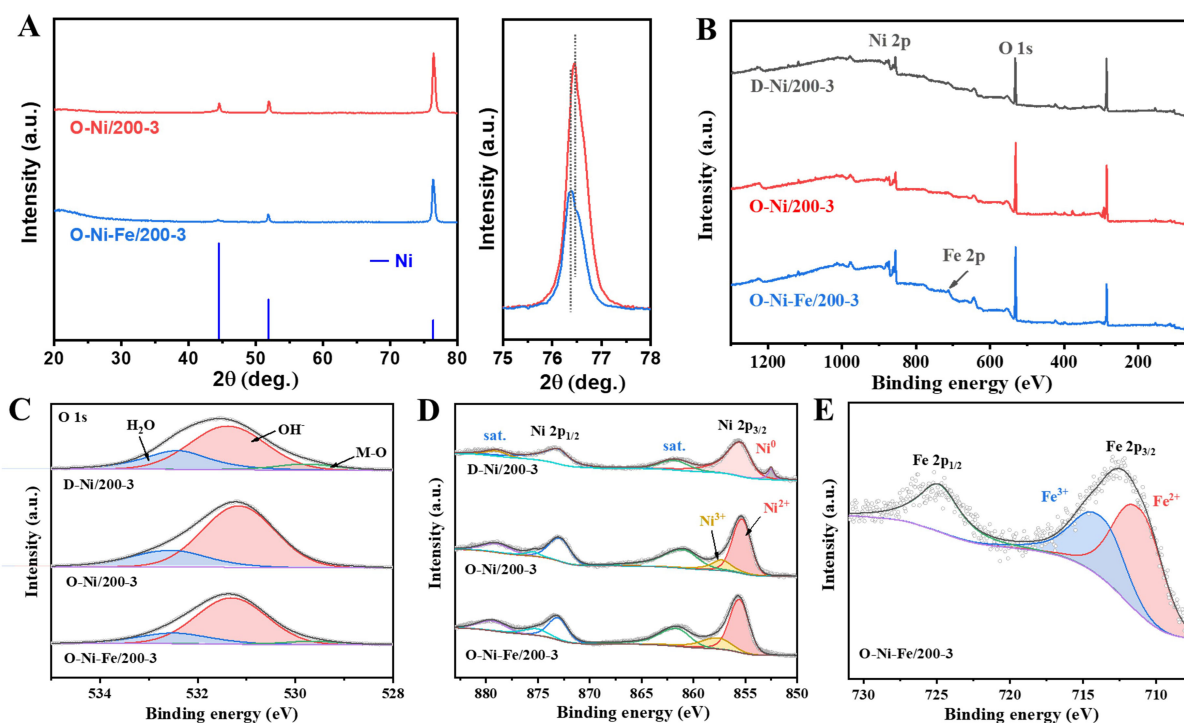


Figure 3. (A) XRD patterns of O-Ni/200-3 and O-Ni-Fe/200-3 and the magnified patterns corresponding to the region at 75°–78° (2 θ). (B) Full-scan XPS spectra and deconvoluted XPS spectra of (C) O 1s, (D) Ni 2p and (E) Fe 2p. XRD: X-ray diffraction; XPS: X-ray photoelectron spectroscopy.

From the above analyses, it can be concluded that a Ni(OH)₂ layer is formed via CV cycling in 0.1 M KOH. The surface SEM images present a rough layer on both O-Ni/200-3 and O-Ni-Fe/200-3, compared with the relatively smooth structure before electrooxidation [Figure 4A and B]. The HRTEM image [Figure 4C] obtained from the boundary area between the dealloyed and un-dealloyed zones (marked in the HAADF image of Figure 4E) of O-Ni-Fe/200-3 displays the (101) lattice plane of Ni(OH)₂ and the (111) lattice plane from Ni. The SAED spectrum from the boundary area further proves the existence of Ni(OH)₂ with diffraction rings from the (101) and (111) lattice planes of Ni(OH)₂ [Figure 4D]. The elemental distribution suggests Fe incorporation into the surface dealloyed zones [Figure 4E]. Many point defects can be observed in the dealloyed zone, as marked by the red rectangles in Figure 4C, which might be attributed to the doping of Fe.

LSV curves were obtained in O₂-saturated 1 M KOH to evaluate the OER catalytic performance. The iR-corrected LSV curves in Figure 5A reveal that O-Ni-Fe/200-3 has the best OER activity, followed by O-Ni/200-3, D-Ni/200-3, and Ni foil without any treatment. An overpotential of only 318 mV is needed to activate a current density of 10 mA cm⁻², lower than 356, 361, and 360 mV for O-Ni/200-3, D-Ni/200-3, and Ni foil, respectively [Supplementary Figure 9]. At a higher current density of 100 mA cm⁻², the overpotential for O-Ni-Fe/200-3 is 385 mV, which is also much lower than for other samples. Kou *et al.* demonstrated that a periodic porous 3D electrode could facilitate the bubble release, thereby guaranteeing a high reaction rate at high current densities^[43]. The dealloying approach in this study could create columnar arrays, which might also have the potential to be used at a high current density.

The Tafel slopes derived from the LSV curves can be used to analyze the kinetic features of the OER process. As given in Figure 5B, the Tafel slope of O-Ni-Fe/200-3 is 60.60 mV dec⁻¹, slightly lower than for

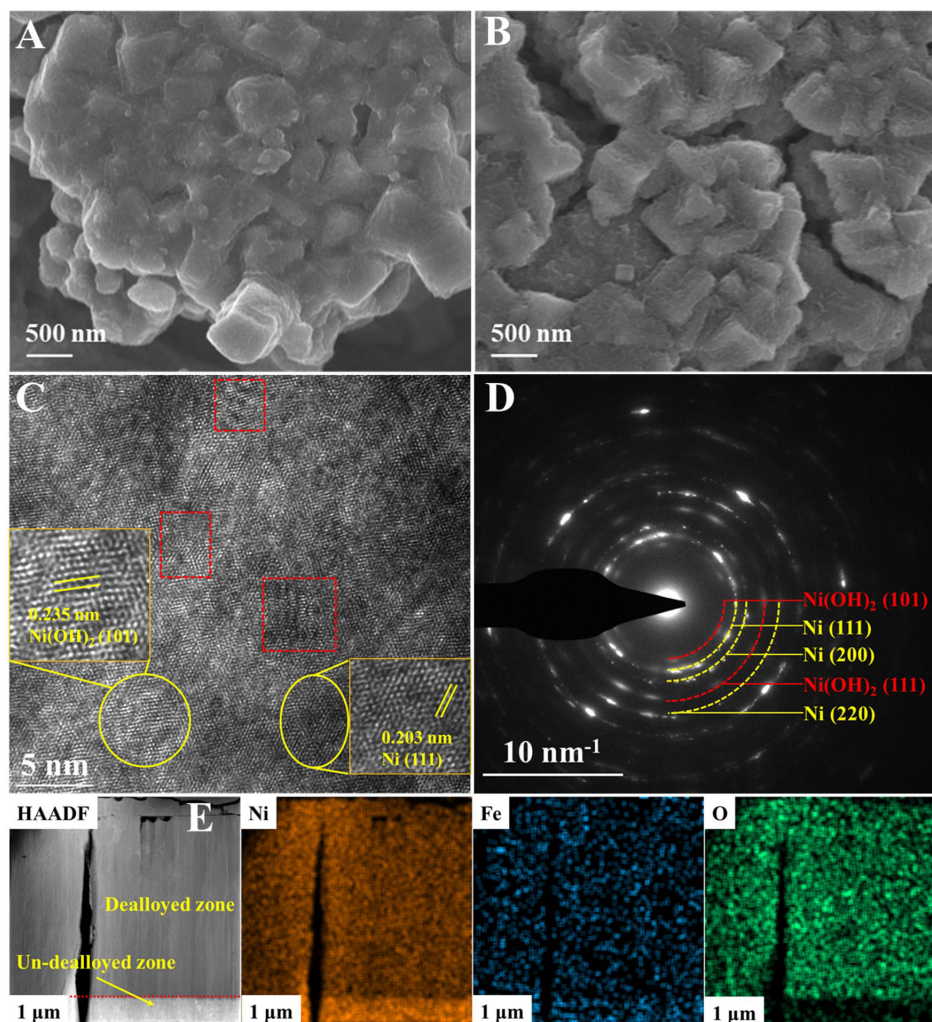


Figure 4. Surface SEM images of (A) O-Ni/200-3 and (B) O-Ni-Fe/200-3. (C) HRTEM, (D) SAED and (E) HAADF and corresponding elemental mapping images of Ni, Fe and O of O-Ni-Fe/200-3. SEM: Scanning electron microscope; HRTEM: high-resolution transmission electron microscopy; SAED: selected area electron diffraction; HAADF: high-angle annular dark field.

O-Ni/200-3 ($66.24 \text{ mV dec}^{-1}$). The Tafel slopes of D-Ni/200-3 and Ni foil are 77.72 and $107.07 \text{ mV dec}^{-1}$, respectively, indicating that the Ni(OH)_2 layer on the surface has a better intrinsic catalytic activity. The Tafel slope is related to the reaction mechanism of a specific system^[5]. In this study, both O-Ni-Fe/200-3 and O-Ni/200-3 have Tafel slopes of $\sim 60 \text{ mV dec}^{-1}$, similar to other Ni(OH)_2 -based catalysts^[25,44,45]. With the formation of Ni(OH)_2 and Fe incorporation, O-Ni-Fe/200-3 is expected to have the most active sites among the catalysts. The electrochemical active surface area (ECSA) estimates the number of active sites and can be obtained from the CV curves scanning in the non-Faradaic potential range at different scanning rates. Figure 5C displays the double-layer capacitance (C_{dl}) values (linearly proportional to ECSA) derived from the CV curves in Supplementary Figure 10A-D. O-Ni-Fe/200-3 has a C_{dl} of 2.07 mF cm^{-2} , higher than the other three catalysts. The ECSAs are calculated according to $\text{ECSA} = (C_{area} \times A / C_{ref})$, where C_{area} is the areal capacitance, A is the geometric area of the electrode (0.25 cm^2), and C_{ref} is the referential areal capacitance of the flat Ni(OH)_2 -based electrode ($80 \mu\text{F cm}^{-2}$)^[46]. The calculated ECSAs of O-Ni-Fe/200-3, O-Ni/200-3, D-Ni/200-3, and Ni foil are 6.47 , 6.03 , 5.62 , and 5.06 cm^2 , respectively, indicating the most active sites for the O-Ni-Fe/200-3 sample.

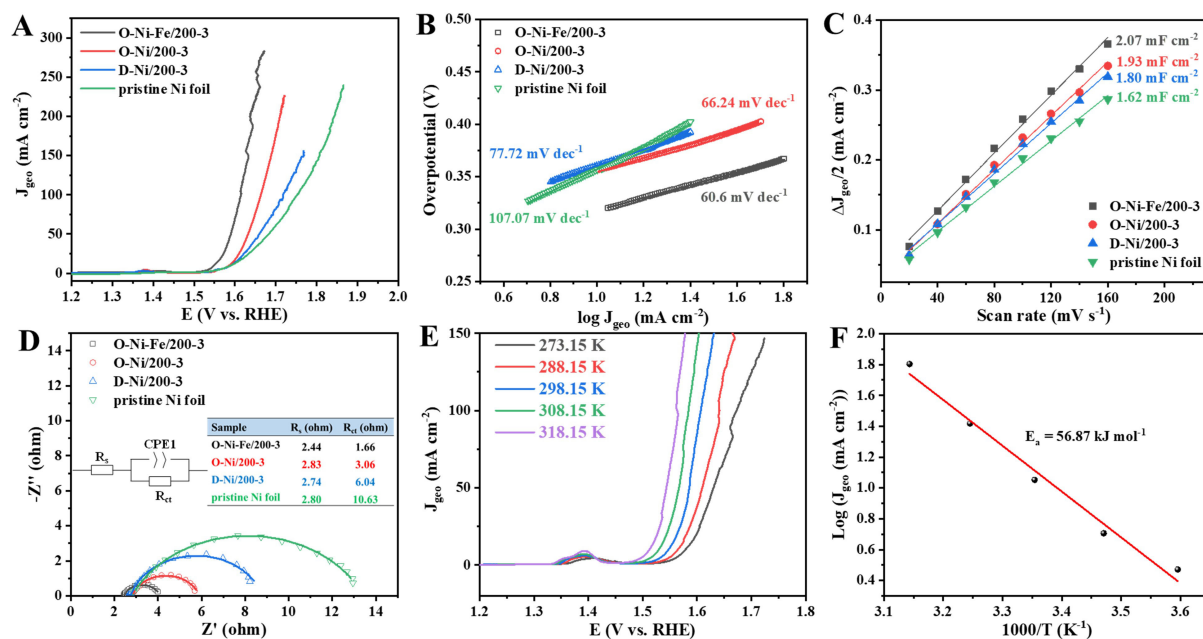


Figure 5. OER activities of different catalysts in 1 M KOH. (A) LSV polarization curves. (B) Tafel plots. (C) Plots of difference between anodic and cathodic current density at 1.188 V vs. RHE as a function of scan rate. (D) Nyquist plots at 1.624 V vs. RHE, where points and lines represent the experimental and simulated data, respectively. (E) LSV curves obtained at different temperatures. (F) Arrhenius plots at 1.53 V vs. RHE. OER: Oxygen evolution reaction; LSV: linear sweep voltammetry; RHE: reversible hydrogen electrode.

EIS was conducted under the same conditions as the LSV tests to probe the catalytic kinetics of the catalysts. The Nyquist plots are fitted based on the equivalent circuit shown as the inset of Figure 5D. The solution resistance (R_s) and charge-transfer resistance (R_{ct}) are listed in the inset table in Figure 5D. O-Ni-Fe/200-3 has the smallest R_{ct} of 1.66 Ω , while Ni foil has the largest R_{ct} of 10.63 Ω due to the lack of Ni(OH)₂ active sites. Despite the significant difference in the R_{ct} , the samples have comparable R_s values, indicating a similar charge transport efficiency. The LSV curves were also obtained at different temperatures to estimate the activation energy (E_a) for the OER. Taking O-Ni-Fe/200-3 as an example, the overpotential to activate the same current density decreases with increasing temperature [Figure 5E]. E_a is calculated through the Arrhenius equation $\frac{\partial \log(J)}{\partial \frac{1}{T}} = -\frac{E_a}{2.3R}$, where J is the current density (mA cm^{-2}) obtained at an overpotential of 300 mV, T is the temperature (K), and R is the gas constant ($8.314 \text{ J mol}^{-1} \cdot \text{K}^{-1}$). The E_a value is 56.87 kJ mol^{-1} for O-Ni-Fe/200-3, as displayed in Figure 5F.

The turnover frequency values (TOF) are applied to assess the catalytic activities, which can be calculated by $\text{TOF} = (J \times A)/(4 \times F \times n)$, where J is the current density (mA cm^{-2}) obtained from the LSV tests, A is the geometric area of the catalysts (0.25 cm^2 in this study), four refers to the number of electrons consumed for evolving one O₂ from water, F is the Faradic constant (96485 C mol⁻¹) and n is the mole value of active sites. The value n can be calculated based on the equation of slope = $(m^2 \times F^2 \times n)/(4 \times R \times T)$, where m is the number of electrons transferred for the oxidation, T is the absolute temperature (298 K), and the other terms are defined as above. The slope can be obtained from the linear relationship between the oxidation peak current and the scanning rate of the CV curves obtained at various scanning rates. Figure 6A and B show the CV curves of O-Ni-Fe/200-3 and O-Ni /200-3 at 1.0–1.6 V vs. RHE at different scanning rates. At ~1.4 V vs. RHE, an oxidation peak is found for each scanning rate. The current density corresponding to the oxidation peak increases obviously with increasing scanning rate. The oxidation peak is generated due to the transformation of Ni²⁺ to Ni³⁺[14,47]. Therefore, the number of active surface sites is calculated based on the linear dependence between the oxidation peak current and scanning rate [Figure 6C][47,48]. Assuming that

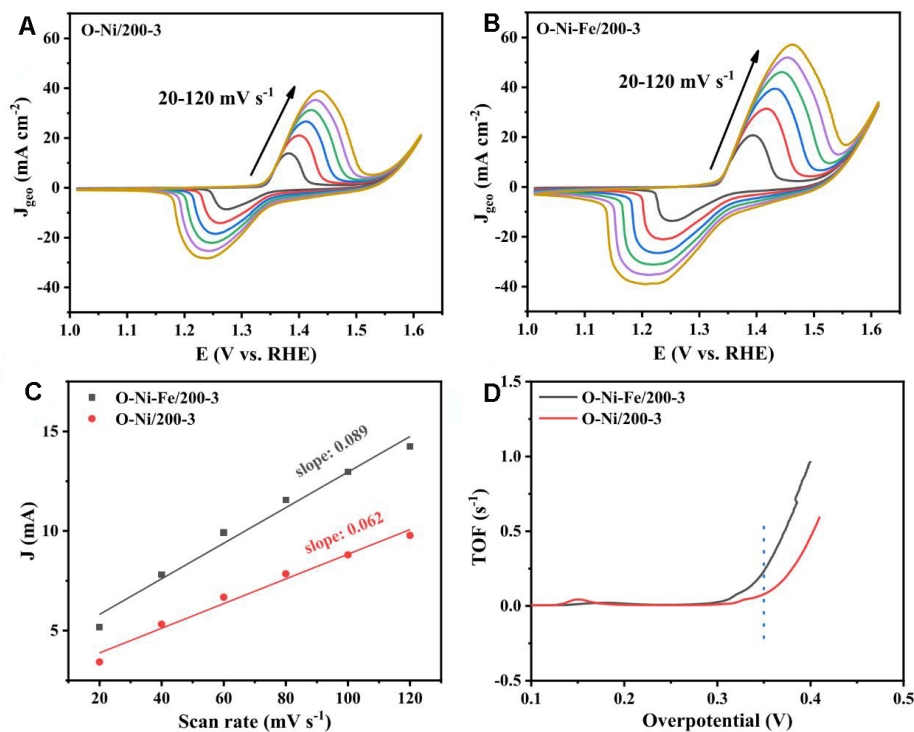


Figure 6. CVs of (A) O-Ni/200-3 and (B) O-Ni-Fe/200-3 at different scan rates (20, 40, 60, 80, 100, and 120 mV s⁻¹) in 1.0 M KOH at 1.024-1.624 V vs. RHE. (C) Oxidation peak current intensity versus scan rate plots. (D) TOF values as a function of overpotential. RHE: Reversible hydrogen electrode; TOF: turnover frequency values.

all active Ni ions contribute to the OER process, TOFs can be calculated based on the number of active surface sites^[49]. The TOF values as a function of overpotential are displayed in Figure 6D. The TOF value is 0.23 and 0.08 s⁻¹ for O-Ni-Fe/200-3 and O-Ni/200-3, respectively, at an overpotential of 350 mV. These results indicate that Fe doping strongly promotes the activity of Ni(OH)₂ on the surface of the catalyst. It is noteworthy that residual Ga (~10 at.% obtained from EDS and XPS) in the dealloyed Ni foil might also affect the electronic structure of Ni and modify the OER performance, as has been proved in Ga-doped Co and Pt materials^[50,51].

The stability during long-term operation is essential to assess the application potential of an OER catalyst. The current density at 1.55 V vs. RHE gradually decreases from 15.8 mA cm⁻² and stabilizes at ~11.9 mA cm⁻² after 7 h (inset of Figure 7A). Before and after the stability test, the CV curves showed comparable current density at the OER potential range [Figure 7A]. The oxidation peak between 1.4 and 1.5 V vs. RHE shifts positively and the current density increases after the stability test. This indicates that the formation of NiOOH occurs more readily after long-term operation. The microstructure and phase composition can be well preserved after the 10 h test [Figure 7B]. A crystal lattice plane distance of 2.139 Å can be observed from the HRTEM image in Figure 7C, corresponding to NiOOH (111). The SAED pattern displays the diffraction rings from Ni(OH)₂ and NiOOH [Figure 7D]. The Ni 2p spectrum of the tested O-Ni-Fe/200-3 is displayed in Figure 7E. The Ni 2p_{3/2} can be fitted into Ni²⁺ and Ni³⁺ and the percentage of Ni³⁺ is 31.8 at.%, higher than 26.7 at.% in the initial O-Ni-Fe/200-3. More Ni³⁺ suggests that more NiOOH might be generated after a long-term test, corresponding to the CV results. The O 1s spectrum further confirms the existence of OH⁻ and Ni-O after the long-term test [Figure 7F]. The above results prove that Fe doping helps the catalyst to maintain its activity after a long-term test via promoting the formation of NiOOH.

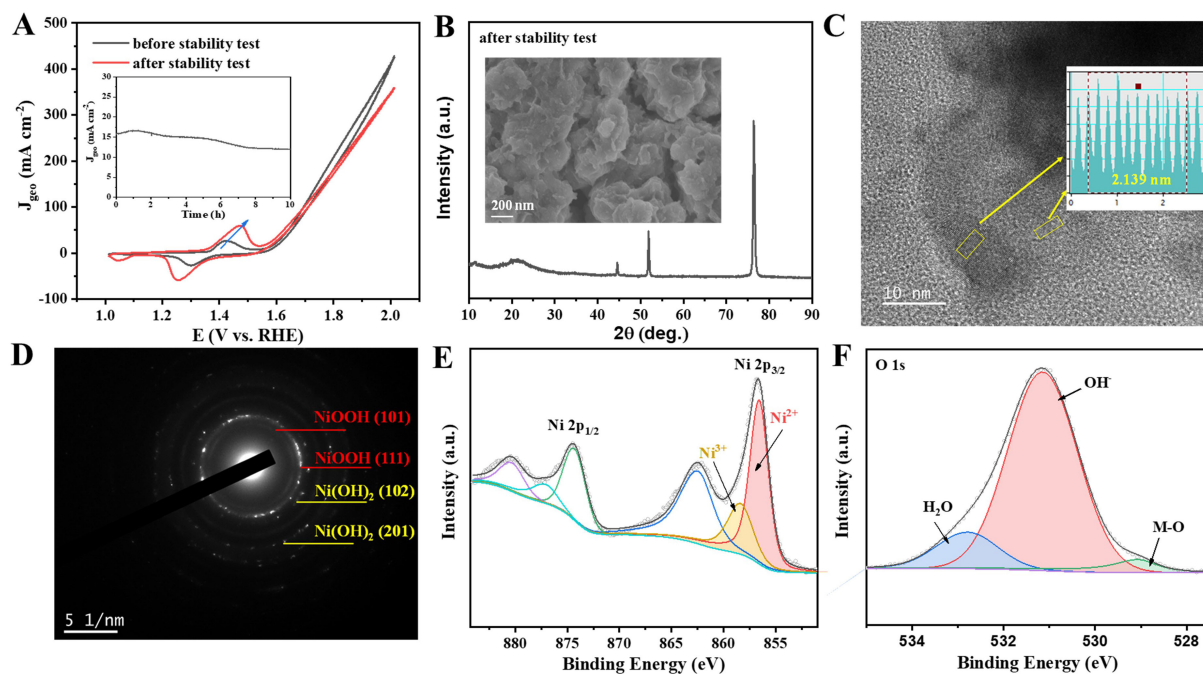


Figure 7. (A) CV curves of O-Ni-Fe/200-3 before and after i-t test; inset is the i-t curve obtained at 1.55 V vs. RHE. (B) XRD of O-Ni-Fe/200-3 after the long-term test; inset is the SEM image. (C) HETEM and (D) SAED of the tested O-Ni-Fe/200-3. (E) Ni 2p and (F) O 1s XPS spectra of tested O-Ni-Fe/200-3. RHE: Reversible hydrogen electrode; XRD: X-ray diffraction; SEM: scanning electron microscope; SAED: selected area electron diffraction; XPS: X-ray photoelectron spectroscopy.

Using the Ga-assisted alloying-dealloying strategy, combined with electrooxidation and Fe doping, a self-supporting $\text{Ni}(\text{OH})_2$ -based catalyst can be achieved for OER applications. In future research, more adjustments to the alloying-dealloying process and the precise control of the Fe-doping amount are expected to enhance the catalytic activity and stability further.

CONCLUSION

This study demonstrates that Ga-assisted alloying-dealloying can be a powerful approach to fabricating self-supporting $\text{Ni}(\text{OH})_2$ -based OER catalysts. By controlling the annealing temperature and time, different Ga-Ni phases can be obtained, which further affect the microstructure of the dealloyed materials. Through further electrooxidation in the Fe^{3+} -containing electrolyte, a Fe-doped $\text{Ni}(\text{OH})_2$ layer was generated on dealloyed Ni foil (O-Ni-Fe/200-3). With an overpotential of 318 mV@10 mA cm^{-2} and a Tafel slope of 60.60 mV dec^{-1} , the O-Ni-Fe/200-3 electrode has an excellent performance in OER catalysis. Under a constant potential, the 10 h i-t test proved its good stability towards the OER in alkaline electrolytes. Fe doping promotes the formation of highly active NiOOH, which might be attributed to the better OER performance. This study sheds light on the controllable surface alloying-dealloying-electrooxidation strategy to fabricate self-supporting Fe-doped $\text{Ni}(\text{OH})_2$ OER catalysts.

DECLARATIONS

Authors' contributions

Project administration, conceptualization, supervision: Zhang C

Manuscript writing: Wang Z, Liang P

Manuscript revision and funding acquisition: He X, Zhang Z, Zhang C

Performed data acquisition and material support: Wang Z, Li Z, Chao Y, Cui Y

Availability of data and materials

Not applicable.

Financial support and sponsorship

This work was supported by the National Natural Science Foundation of China (No. 51901161), Natural Science Foundation of Guangdong Province (No. 2021A1515011955), College Innovation Team Project of Guangdong Province (No. 2021KCXTD042), Major Projects of Guangdong Education Department for Foundation Research and Applied Research (No. 2020ZDZX2063; No. 2019KZDXM065), Wuyi University-Hong Kong-Macau Joint Research and Development Fund (No. 2019WGALH06).

Conflicts of interest

All authors declared that there are no conflicts of interest.

Ethical approval and consent to participate

Not applicable.

Consent for publication

Not applicable.

Copyright

© The Author(s) 2022.

REFERENCES

1. Roger I, Shipman MA, Symes MD. Earth-abundant catalysts for electrochemical and photoelectrochemical water splitting. *Nat Rev Chem* 2017;1. DOI
2. Chu S, Majumdar A. Opportunities and challenges for a sustainable energy future. *Nature* 2012;488:294-303. DOI PubMed
3. Zhang B, Wang L, Cao Z, et al. High-valence metals improve oxygen evolution reaction performance by modulating 3d metal oxidation cycle energetics. *Nat Catal* 2020;3:985-92. DOI
4. Wei C, Rao RR, Peng J, et al. Recommended practices and benchmark activity for hydrogen and oxygen electrocatalysis in water splitting and fuel cells. *Adv Mater* 2019;31:e1806296. DOI PubMed
5. Suen NT, Hung SF, Quan Q, Zhang N, Xu YJ, Chen HM. Electrocatalysis for the oxygen evolution reaction: recent development and future perspectives. *Chem Soc Rev* 2017;46:337-65. DOI PubMed
6. Xue Q, Bai X, Zhao Y, et al. Au core-PtAu alloy shell nanowires for formic acid electrolysis. *J Energy Chem* 2022;65:94-102. DOI
7. Ding Y, Cao K, He J, et al. Nitrogen-doped graphene aerogel-supported ruthenium nanocrystals for pH-universal hydrogen evolution reaction. *Chinese J Catal* 2022;43:1535-43. DOI
8. Hu F, Wang H, Zhang Y, et al. Designing highly efficient and long-term durable electrocatalyst for oxygen evolution by coupling B and P into amorphous porous NiFe-based material. *Small* 2019;15:e1901020. DOI PubMed
9. Gong M, Dai H. A mini review of NiFe-based materials as highly active oxygen evolution reaction electrocatalysts. *Nano Res* 2015;8:23-39. DOI
10. Zhu YP, Ma TY, Jaroniec M, Qiao SZ. Self-templating synthesis of hollow Co₃O₄ microtube arrays for highly efficient water electrolysis. *Angew Chem Int Ed* 2017;56:1324-8. DOI
11. Suntivich J, Gasteiger HA, Yabuuchi N, Nakanishi H, Goodenough JB, Shao-horn Y. Design principles for oxygen-reduction activity on perovskite oxide catalysts for fuel cells and metal-air batteries. *Nature Chem* 2011;3:546-50. DOI PubMed
12. Peng S, Gong F, Li L, et al. Necklace-like multishelled hollow spinel oxides with oxygen vacancies for efficient water electrolysis. *J Am Chem Soc* 2018;140:13644-53. DOI PubMed
13. Wu Z, Lu XF, Zang SQ, Lou XW. Non-noble-metal-based electrocatalysts toward the oxygen evolution reaction. *Adv Funct Mater* 2020;30:1910274. DOI
14. Trotochaud L, Young SL, Ranney JK, Boettcher SW. Nickel-iron oxyhydroxide oxygen-evolution electrocatalysts: the role of intentional and incidental iron incorporation. *J Am Chem Soc* 2014;136:6744-53. DOI PubMed
15. Xuan C, Lei W, Wang J, et al. Sea urchin-like Ni-Fe sulfide architectures as efficient electrocatalysts for the oxygen evolution reaction. *J Mater Chem A* 2019;7:12350-7. DOI

16. Zhou W, Wu X, Cao X, et al. Ni₃S₂ nanorods/Ni foam composite electrode with low overpotential for electrocatalytic oxygen evolution. *Energy Environ Sci* 2013;6:2921. DOI
17. Friebel D, Louie MW, Bajdich M, et al. Identification of highly active Fe sites in (Ni,Fe)OOH for electrocatalytic water splitting. *J Am Chem Soc* 2015;137:1305-13. DOI PubMed
18. Zhang F, Shi Y, Xue T, Zhang J, Liang Y, Zhang B. In situ electrochemically converting Fe₂O₃-Ni(OH)₂ to NiFe₂O₄-NiOOH: a highly efficient electrocatalyst towards water oxidation. *Sci China Mater* 2017;60:324-34. DOI
19. Corrigan DA. The catalysis of the oxygen evolution reaction by iron impurities in thin film nickel oxide electrodes *J Electrochem Soc* 1987;134:377-84. DOI
20. Klaus S, Cai Y, Louie MW, Trotochaud L, Bell AT. Effects of Fe electrolyte impurities on Ni(OH)₂/NiOOH structure and oxygen evolution activity. *J Phys Chem C* 2015;119:7243-54. DOI
21. Sun H, Yan Z, Liu F, Xu W, Cheng F, Chen J. Self-supported transition-metal-based electrocatalysts for hydrogen and oxygen evolution. *Adv Mater* 2020;32:e1806326. DOI PubMed
22. Pi Y, Shao Q, Wang P, et al. Trimetallic oxyhydroxide coraloids for efficient oxygen evolution electrocatalysis. *Angew Chem Int Ed* 2017;56:4502-6. DOI PubMed
23. Zhu Y, Liu Y, Ren T, Yuan Z. Self-supported cobalt phosphide mesoporous nanorod arrays: a flexible and bifunctional electrode for highly active electrocatalytic water reduction and oxidation. *Adv Funct Mater* 2015;25:7337-47. DOI
24. Xu K, Wang F, Wang Z, et al. Component-controllable WS_{(2(1-x))}Se_(2x) nanotubes for efficient hydrogen evolution reaction. *ACS Nano* 2014;8:8468-76. DOI PubMed
25. Kou T, Wang S, Hauser JL, et al. Ni foam-supported Fe-Doped β-Ni(OH)₂ nanosheets show ultralow overpotential for oxygen evolution reaction. *ACS Energy Lett* 2019;4:622-8. DOI
26. Kou T, Chen M, Wu F, et al. Carbon doping switching on the hydrogen adsorption activity of NiO for hydrogen evolution reaction. *Nat Commun* 2020;11:590. DOI PubMed PMC
27. Hu F, Zhu S, Chen S, et al. Amorphous metallic NiFeP: a conductive bulk material achieving high activity for oxygen evolution reaction in both alkaline and acidic media. *Adv Mater* 2017;29:1606570. DOI PubMed
28. Zheng D, Zhao F, Li Y, et al. Flexible NiO micro-rods/nanoporous Ni/metallic glass electrode with sandwich structure for high performance supercapacitors. *Electrochim Acta* 2019;297:767-77. DOI
29. Wang Z, Gao H, Niu J, Zhang C, Zhang Z. Transforming bulk metals into metallic nanostructures: a liquid-metal-assisted top-down dealloying strategy with sustainability. *ACS Sustainable Chem Eng* 2019;7:3274-81. DOI
30. Wang Z, Wang Y, Gao H, et al. "Painting" nanostructured metals-playing with liquid metal. *Nanoscale Horiz* 2018;3:408-16. DOI PubMed
31. Zhang J, Dong C, Wang Z, et al. Flexible, self-supported hexagonal β-Co(OH)₂ nanosheet arrays as integrated electrode catalyzing oxygen evolution reaction. *Electrochim Acta* 2018;284:495-503. DOI
32. Liu Y, Bliznakov S, Dimitrov N. Factors controlling the less noble metal retention in nanoporous structures processed by electrochemical dealloying. *J Electrochem Soc* 2010;157:K168. DOI
33. Zhang J, Bai Y, Zhang C, et al. Hybrid Ni(OH)₂/FeOOH@NiFe nanosheet catalysts toward highly efficient oxygen evolution reaction with ultralong stability over 1000 hours. *ACS Sustainable Chem Eng* 2019;7:14601-10. DOI
34. Stevens MB, Trang CDM, Enman LJ, Deng J, Boettcher SW. Reactive Fe-sites in Ni/Fe (Oxy)hydroxide are responsible for exceptional oxygen electrocatalysis activity. *J Am Chem Soc* 2017;139:11361-4. DOI PubMed
35. Ren JT, Yuan GG, Weng CC, Chen L, Yuan ZY. Uniquely integrated Fe-doped Ni(OH)₂ nanosheets for highly efficient oxygen and hydrogen evolution reactions. *Nanoscale* 2018;10:10620-8. DOI PubMed
36. Son YJ, Kawashima K, Wygant BR, et al. Anodized nickel foam for oxygen evolution reaction in Fe-free and unpurified alkaline electrolytes at high current densities. *ACS Nano* 2021;15:3468-80. DOI PubMed
37. Wang Z, Zhang X, Liu X, et al. Bimodal nanoporous NiO@Ni-Si network prepared by dealloying method for stable Li-ion storage. *J Power Sources* 2020;449:227550. DOI
38. Wu Y, Zhao MJ, Li F, Xie J, Li Y, He JB. Trace Fe incorporation into Ni-(oxy)hydroxide stabilizes Ni³⁺ sites for anodic oxygen evolution: a double thin-layer study. *Langmuir* 2020;36:5126-33. DOI PubMed
39. Mansour AN. Characterization of β-Ni(OH)₂ by XPS. *Surf Sci Spectra* 1994;3:239-46. DOI
40. Biesinger MC, Payne BP, Grosvenor AP, Lau LW, Gerson AR, Smart RS. Resolving surface chemical states in XPS analysis of first row transition metals, oxides and hydroxides: Cr, Mn, Fe, Co and Ni. *Appl Surf Sci* 2011;257:2717-30. DOI
41. Smith RD, Prévot MS, Fagan RD, Trudel S, Berlinguette CP. Water oxidation catalysis: electrocatalytic response to metal stoichiometry in amorphous metal oxide films containing iron, cobalt, and nickel. *J Am Chem Soc* 2013;135:11580-6. DOI PubMed
42. Yamashita T, Hayes P. Analysis of XPS spectra of Fe²⁺ and Fe³⁺ ions in oxide materials. *Appl Surf Sci* 2008;254:2441-9. DOI
43. Kou T, Wang S, Shi R, et al. Periodic porous 3D electrodes mitigate gas bubble traffic during alkaline water electrolysis at high current densities. *Adv Energy Mater* 2020;10:2002955. DOI
44. Zhang C, Xie Z, Liang Y, et al. Morphological and compositional modification of β-Ni(OH)₂ nanoplates by ferrihydrite for enhanced oxygen evolution reaction. *Int J Hydrog Energy* 2021;46:17720-30. DOI
45. Lyons MEG, Doyle RL, Godwin I, O'Brien M, Russell L. Hydrous nickel oxide: redox switching and the oxygen evolution reaction in aqueous alkaline solution. *J Electrochem Soc* 2012;159:H932-44. DOI
46. Stevens MB, Enman LJ, Batchellor AS, et al. Measurement techniques for the study of thin film heterogeneous water oxidation

- electrocatalysts. *Chem Mater* 2017;29:120-40. [DOI](#)
47. Guo X, Kong R, Zhang X, Du H, Qu F. Ni(OH)₂ Nanoparticles embedded in conductive microrod array: an efficient and durable electrocatalyst for alkaline oxygen evolution reaction. *ACS Catal* 2018;8:651-5. [DOI](#)
 48. Zou X, Goswami A, Asefa T. Efficient noble metal-free (electro)catalysis of water and alcohol oxidations by zinc-cobalt layered double hydroxide. *J Am Chem Soc* 2013;135:17242-5. [DOI](#) [PubMed](#)
 49. Surendranath Y, Kanan MW, Nocera DG. Mechanistic studies of the oxygen evolution reaction by a cobalt-phosphate catalyst at neutral pH. *J Am Chem Soc* 2010;132:16501-9. [DOI](#) [PubMed](#)
 50. Zhang S, Zhang J, Liang P, Zhang C, Kou T, Zhang Z. Corrosion engineering derived Ga doped CoSe₂ nanosheets intrinsically active for oxygen evolution reaction. *J Power Sources* 2021;497:229895. [DOI](#)
 51. Wang Y, Wang Z, Zhang J, et al. A self-supported nanoporous PtGa film as an efficient multifunctional electrocatalyst for energy conversion. *Nanoscale* 2018;10:17070-9. [DOI](#) [PubMed](#)